Aalborg Universitet

Radiation-Pattern Reconfigurable Phased Array with p-i-n Diodes Controlled for 5G Mobile Terminals

Zhang, Jin; Zhang, Shuai; Ying, Zhinong; Morris, Arthur; Pedersen, Gert Frølund

Radiation-Pattern Reconfigurable Phased Array With p-i-n Diodes Controlled for 5G Mobile Terminals

Jin Zhang , Shuai Zhang , *Senior Member, IEEE*, Zhinong Ying , *Senior Member, IEEE*, Arthur S. Morris, III, *Fellow, IEEE*, and Gert Frølund Pedersen

Abstract—A p-i-n diodes-controlled radiation-pattern reconfigurable phased array for fifth-generation (5G) handsets is proposed in this article. The proposed beam scanning and switching hybrid system can significantly reduce the number of arrays and transmit–receive (TR) components when compared with multiarray systems while keeping the same spatial coverage. The array has wide working band from 24 to 27.5 GHz, which can cover the allocated 5G band for Europe. The four-element array is planar with a small clearance of only 4 mm, which is suitable for most of the current mobile phones. Each reconfigurable array element is fed by one shielded stripline and has three switchable radiation patterns: two broadside directions and one endfire direction. The beam switching is realized by applying two reconfigurable directors on both sides of the dipole, which also reduces the antenna profile. The directors are activated when the p-i-n diodes are at OFF mode, which minimizes the energy loss on the p-i-n diodes. The parasitic influence of the p-i-n diodes, the soldering process, and mobile environment are discussed in detail. The measured results show good agreement with the simulations.

Index Terms—Fifth generation (5G) antenna for mobile terminals, phased array, radiation-pattern reconfigurable antenna.

I. INTRODUCTION

THE research on millimeter-wave (mm-wave) fifth-generation (5G) mobile antennas has focused on the phased arrays and beam switching antennas to maximize the gain within the wireless link budget [1]–[3]. As a result, the spatial coverage decreases because of the narrow beams and the limit of scanning angle. The concept of coverage efficiency is introduced in [4] to describe the performance of antenna gain and coverage in the space. To further increase the coverage efficiency of the phased arrays, beam switching between several subarrays is one of the solutions [5], [6].

In [5], each of the three subarrays covers a different area in the space. It gives an idea about combining beam switching and beam scanning but does not provide a realization of the feeding network. The problem is solved in [6], which realizes the beam switching and scanning on a single layer printed circuit board (PCB). The surface current has different distributions on the ground plane depending on which subarray is chosen to work, which, as a result, leads to different main beam directions. This method is simple, but the 24 feeding ports and transmission lines still make this design hard to integrate inside a mobile phone. At the same time, the clearance of 10.5 mm is not compatible with the expanding screen. Instead of using three arrays, Zhang *et al.* [7] realize three-dimension (3-D) radiation pattern reconfiguration by only one array with reconfigurable array elements. Comparing with [5] and [6], it solves the feeding problem in [5], and the number of feeding ports shrinks from 24 to 8. However, the bandwidth in [7] is too narrow due to the strong resonant structure, which also limits its application in the 5G communication systems. Moreover, the antenna structure is complicated, and mounting the p-i-n diodes in the middle layer is difficult for the PCB fabrication and dc controlling.

Many works about the radiation-pattern reconfigurable antennas are done at low frequencies. For instance, a beam scanning reflectarray in [8] and a diffraction antenna in [9] are realized by tuning the capacitance of varactors. A beam switching quasi-Yagi dipole antenna is proposed in [10] by changing the length of the balun and the directors. The *E*-plane beam can operate in three directions: −20°, 0°, and 20°. However, the beam switching range is not big enough, and the directors take large space. Another method to get switchable beams is to combine and switch among different resonant modes on one radiator [11]–[13]. However, large apertures are required to support higher order modes, and the bandwidth of each mode is narrow. Modifying the parasitic parts near the radiator can influence its beam direction, which is also a common way of realizing beam switching antennas. By applying switchable directors and reflectors to the radiator, the main beam can switch in different directions in [14]–[17]. Still, the parasitic elements require space around the active antenna, and some of them are even realized in the 3-D structure. Even though all those examples are made for low frequencies, they have potential for mm-wave

This article has been accepted for inclusion in a future issue of this journal. Content is final as presented, with the exception of pagination.

2 IEEE TRANSACTIONS ON MICROWAVE THEORY AND TECHNIQUES

bands applications. Since the quarter wavelength dipole-director distance is comparable with the thickness of the standard substrates, it is possible to simplify the fabrication.

However, the problem of loss arises. In the above-mentioned articles, the p-i-n diodes turn ON to let the current go through, which can seriously impact the antenna total efficiency in the mm-waveband. To reduce the loss, some of the beam switching antennas in the mm-waveband use mechanical or optical control and special material or diodes [18]–[23]. In this way, the antennas have good efficiency, but they are still not suitable for mobile phones due to the switching speed, the size, and the cost. The p-i-n diodes are used to build reconfigurable transmit arrays in [24]–[26], which turns out that the loss can be reduced under the premise of good designs.

In this article, a hybrid beam scanning and switching antenna array system is proposed, in which pattern-reconfigurable antennas are used as array elements. Comparing with the conventional multiarray beam scanning system, it saves up to two thirds of components but can still reach the same spatial coverage. The beam scanning is realized by the phase-shifting system, and the beam switching is realized by pattern-reconfigurable array elements. The combinations of two reconfigurable strips on each side of one array element direct to three different beam directions (0°, 90°, and 180°) in the θ plane, while the beam scanning operates in the ϕ plane. The strip is activated as a director when the p-i-n diodes are at "OFF" state. Therefore, the energy loss on the p-i-n diodes is minimized due to the negligible through current level. The same method can be further applied to other reconfigurable antennas and circuits design in mm-waveband. A four-element array is also constructed with the proposed reconfigurable array elements. The simulations and measurements show that the proposed antenna and array work with good efficiency.

We stress the fact that the novelties of this article are threefold, as given in the following.

1) The realization of beam switching and scanning array for a hybrid antenna system provides a large spatial coverage over a wideband and reduces the numbers of antennas and transmit–receive (TR) components.
2) The realization of pattern-reconfigurable array element achieves low profile, small clearance, and high efficiency.
3) The realistic influences, for instance, the soldering process and the mobile phone environment, are discussed.

This article is organized as follows. Section II compares the proposed system framework with the conventional antenna system for 5G handsets. Section III introduces the design of the radiation-pattern reconfigurable array element. Section IV presents the performance of the four-element phased array with the reconfigurable array elements. Section V studies the impact of the realistic operating environment. This article is concluded in Section VI. CST STUDIO SUITE 2018 is used for all the simulations in this article.

II. COMPARATIVE FRAMEWORK

In this section, a comparison of transceiver antenna array system architectures in a 5G mm-wave mobile device
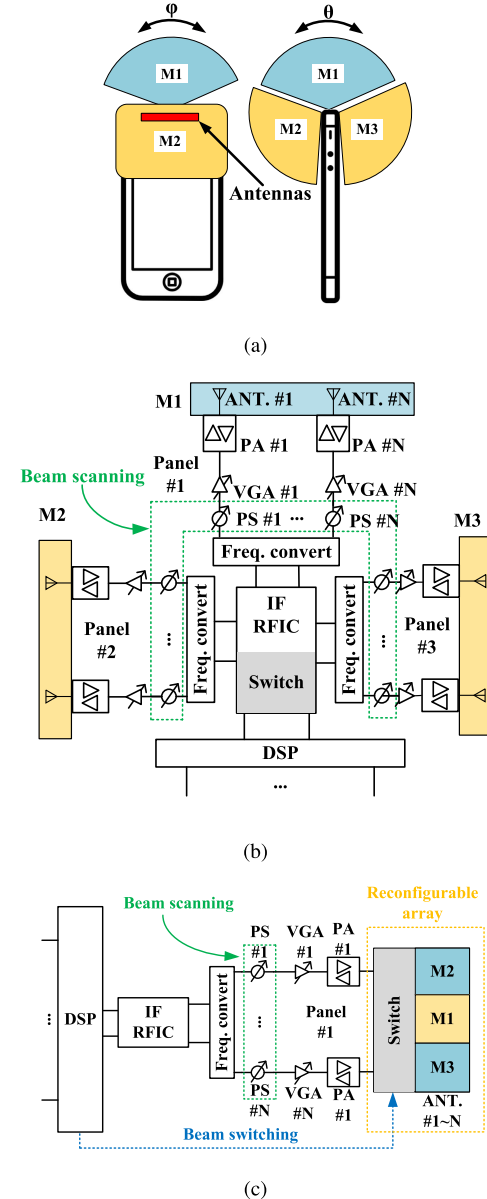
Fig. 1. Two different transceiver antenna array system architectures. (a) Scanning mechanism. (b) Multiple arrays beam scanning system. (c) Beam scanning and switching hybrid system.

is introduced. In order to reach the spatial coverage requirements in [27], a two-dimension (2-D) beam scanning array is highly recommended, as shown in Fig. 1(a). Each array covers a different sector in the space, which is marked as M1, M2, and M3. Two different array system architectures can realize this 2-D scanning pattern. Fig. 1(b) represents the system with only beam scanning based on the phase-shifting system. Each antenna panel contains one independent linear phased array, which covers a specific area: M1, M2, or M3. Therefore, three signal panels are required in this system. Each of the panels consists of N array elements (ANT.), power amplifiers, variable gain amplifiers, phase shifters (PSs), and frequency converter. All the PSs are controlled by the same baseband digital signal processor (DSP) in order to realize the beam scanning function. The intermediate frequency (IF)

This article has been accepted for inclusion in a future issue of this journal. Content is final as presented, with the exception of pagination.

ZHANG *et al.*: RADIATION-PATTERN RECONFIGURABLE PHASED ARRAY WITH p-i-n DIODES CONTROLLED

3

radio frequency integrated circuit (RFIC) contains a function of switch, which chooses one of the three arrays to work. Fig. 1(c) represents a beam scanning and switching hybrid array system, in which only one linear array is required. Each array element has three switchable radiation modes, which allow the coverage of the array switching between M1, M2, and M3. The beam scanning is realized in the same way as the conventional system in Fig. 1(b). For the beam switching, instead of choosing a different array, one of the three modes of the same array is chosen to work. The switching components are mounted on the antenna, and their control is still integrated into the IF RFIC. In this article, p-i-n diodes are chosen as the switching components due to the ease of control. Two independent dc feedings are required, which corresponds to three switching states: one endfire mode and two broadside modes. The dc power for p-i-n diodes and PSs is provided by DSP. Comparing with the multiple array system, the proposed hybrid system can reach the same spatial coverage but requires only one third of the antennas, PS-groups, and RF-chains. The complexity and cost of the whole antenna system is much reduced.

III. RADIATION-PATTERN RECONFIGURABLE ARRAY ELEMENT

A radiation-pattern reconfigurable dipole antenna as the array element will be introduced in this section. It includes the following parts: 1) the antenna configuration; 2) the working principle of the three switching modes; 3) the realization of the three modes by switching with mm-wave p-i-n diodes; 4) the simulated antenna element performance; and 5) a comparison with dipole antenna backed with a conductor. Many analyses are chosen at 28 GHz as an example, while the same working principle applies in other bands.

A. Antenna Configuration

In order to reduce the cost, the 5G ICs and radiating part of the hybrid antenna system can be fabricated by different materials [28]. Moreover, the antenna total efficiency is less affected by modifying the radiating part on low loss materials. Therefore, in the following, we will mainly focus on the reconfigurable antenna systems instead of the 5G IC. The antenna configuration is shown in Fig. 2. The antenna is realized in a multilayer structure, which includes three substrate layers (Sub.1, Sub.2, and Sub.3) and two prepreg layers (P1 and P2). The material of substrate layers is Rogers RO4350B ($\epsilon_r = 3.66$ and $\tan \delta = 0.0037$). The materials of P1 and P2 are Arlon 49N ($\epsilon_r = 4.8$ and $\tan \delta = 0.025$) and Rogers RO4450F ($\epsilon_r = 3.52$, $\tan \delta = 0.004$), respectively. The metallic layers (M1– M5) are made of copper ($\sigma_{\text{copper}} = 5.8 \times 10^7$ S/m). The thickness of the metallic layers is 18 μm. The layers are demonstrated in different colors. The structures of all layers are shown in the exploded view in Fig. 2(a). The layer stack-up and the depth of vias are shown in the cross-sectional view in Fig. 2(b). Dipole antennas are chosen as array elements due to their small clearance and wideband. The dipole is printed on layer M2, and the two directors are on layer M1 and M5. The size and position of the directors
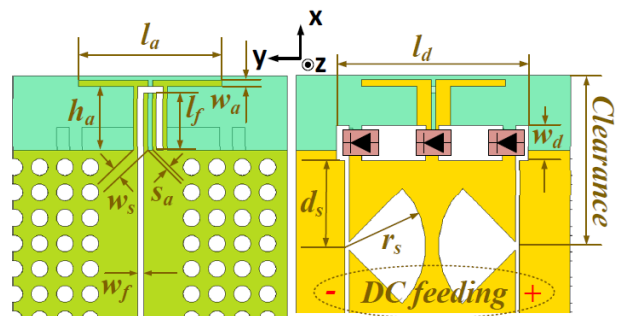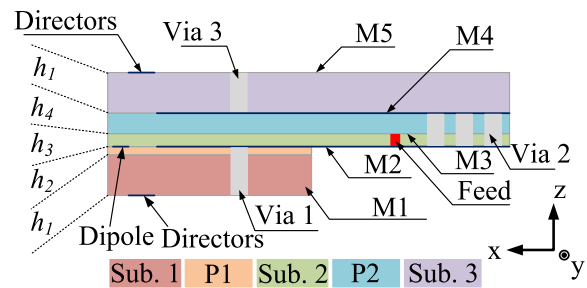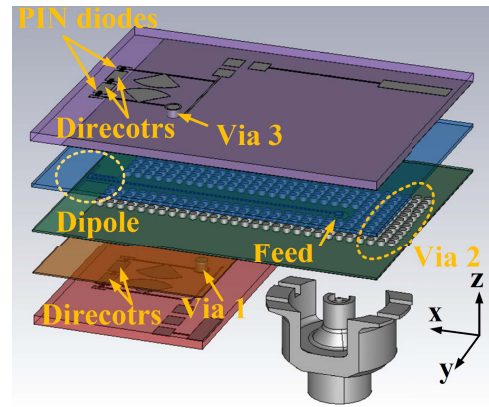
Fig. 2. Antenna configuration. (a) Exploded view. (b) Cross-sectional view. (c) Dimensions.

TABLE I
DIMENSIONS OF THE PROPOSED ANTENNA. (UNITS: mm)

l_a	w_a	h_a	s_a	l_f	w_f	l_d	W_s
3.4	0.15	1.5	0.1	1.35	0.15	4.5	0.35
w_d	d_s	r_s	h_1	h_2	h_3	h_4	
0.8	2	1.85	0.508	0.075	0.1	0.2	

are the same. The measures of the dipole antenna are shown in Fig. 2(c). All the dimensions are summarized in Table I. The clearance represents the area needs to be reserved on the ground plane or the screen in order to guarantee the antenna performance. The clearance for the proposed antenna is 4 mm according to the discussion in Section V-B.

The dipole antenna is fed by a stripline on M3, which is connected with an MMPX connector through a via (Feed) on Sub.2. M2 and M4 are the ground planes, which are connected

This article has been accepted for inclusion in a future issue of this journal. Content is final as presented, with the exception of pagination.

4   IEEE TRANSACTIONS ON MICROWAVE THEORY AND TECHNIQUES

with each other with many vias (Via 2). The feeding trip line is shielded in a cavity formed by M2, M4, and Via 2. The shielding of the feeding line avoids the undesired surface wave propagation and radiation, which can decrease the interaction between the antenna elements and lower the loss of the transmission line. The radiation pattern reconfiguration is realized by two reconfigurable directors. Each director is loaded with three p-i-n diodes and the corresponding dc control networks. The dc feeding lines are connected to the two ends of the director, as shown in Fig. 2(c). The sector patches work as RF chocks. The radius of the sector patches (r_s) is the quarter-wavelength of 28 GHz. The parts of the dc feeding lines after the sector patches have limited influence on the radiation. They can be shortened, extended, or bent, and then be connected to the main PCB at any convenient position. The DSP module is required to provide two independent dc signals, which correspond to three working modes of the antenna. In addition, the dc feeding lines of all the array elements are connected together on each side. Therefore, the dc control for the array is the same as that for a single antenna. The increasing of array elements will not increase the complexity of the dc control. The three p-i-n diodes on one director have the same working state and are controlled by one dc source; therefore, for each antenna, two independent dc sources are required.

B. Working Principle of the Three Switching Modes

The proposed antenna is expected to have three working modes, which correspond to three switchable radiation patterns: one endfire mode and two broadside modes. For each mode, the main beam direction of the antenna is the result of the joint influence of the ground plane and the directors. The cross-sectional view of the upper half part of the antenna is shown in Fig. 3(a) to help to explain the working principle.

The endfire mode is simply without the director's effect. D1 represents the main beam direction with the reflection of the ground plane alone. The distance between the dipole and the ground plane is d_2, which is chosen as $\lambda/4$ to get the best gain.

For the broadside mode, the influence of the ground plane still exists. Therefore, a director must be introduced to compensate for the ground plane influence. D2 represents the main beam direction with only the influence of the director. The director is not right over the dipole antenna, so that the distance between the dipole and the director (d_1) can be calculated by the substrate thickness $(h_1 + h_3 + h_4)$ and the x-axis position of the director (d_3).

The dipole and the director can be considered as a Yagi antenna. The gain of this Yagi antenna is a function of director length (l_d) and the separation between the driving element and the director (d_1). The main beam direction of the Yagi antenna (θ) is influenced by (d_3). Therefore, the position of the director (d_3) relates to both the gain and the radiation direction. The desired broadside radiation direction is D3, which is synthesized by D1 and D2. Theoretically, increasing d_3 will decrease θ and, as a consequence, make the broadside beam going more backward $(-x)$. The gain is stable when the separation of the driven element and the director is between
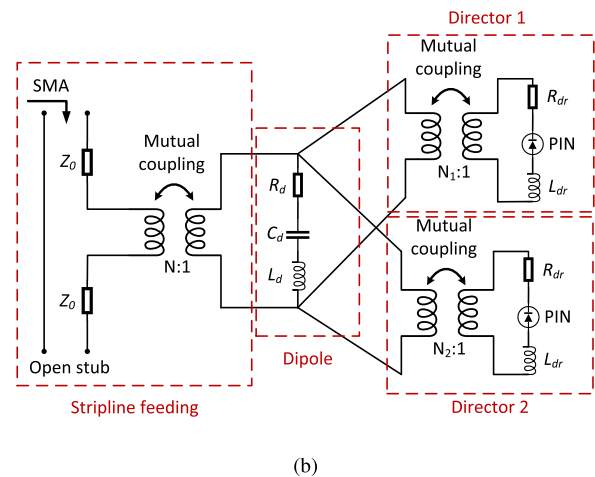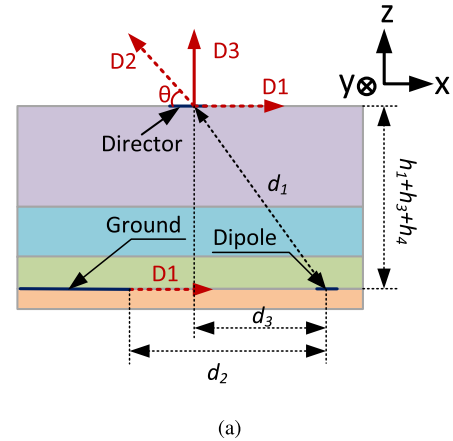

Fig. 3. Working principle. (a) Collective effect of the ground plane and the director. (b) Equivalent circuit of the reconfigurable dipole.

$0.15\lambda_0$ and $0.3\lambda_0$. That means, in principle, the total thickness of the material $(h_1 + h_3 + h_4)$ should be in a certain range. For the millimeter-wave antenna design, most of the standard substrates satisfy this condition. Considering the influence of substrate dielectric constant, the total thickness could be further decreased to below $0.15\lambda_0$. In our design, the suitable value of $h_1 + h_3 + h_4$ is $0.075\lambda_0$ from the simulations. It is an advantage for integrating the proposed antennas into the mobile phones because the low profile and compact structure occupy less space.

Decreasing θ may increase the spatial coverage of the three switchable modes. However, the decrement of θ is limited. When the director is moved from the $+x$-direction to the $-x$-direction, the effect of the director will first increase and then decrease due to the coupling between the dipole and the director will be blocked by the ground plane. The influence of the director is verified in Fig. 4. It shows the radiation patterns of one of the broadside modes at 31 GHz when the director is in different positions. This frequency is chosen as the upper bound of the whole operating band in order to maximize the differences. When d_3 is 0 mm, the director is just over the dipole. When d_3 is 1 mm, the director is between the dipole and the edge of the ground plane. When d_3 is 2 mm, the director is above the ground plane. As we can see, the radiation pattern has a good broadside shape when d_3
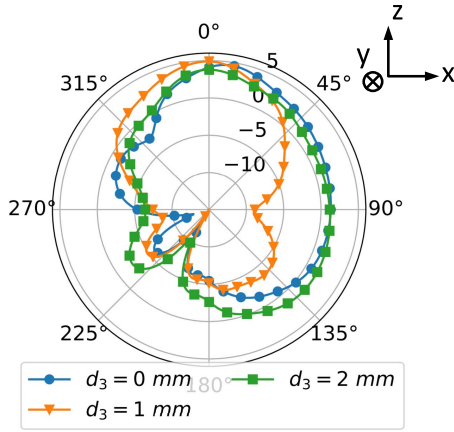
This article has been accepted for inclusion in a future issue of this journal. Content is final as presented, with the exception of pagination.

ZHANG *et al.*: RADIATION-PATTERN RECONFIGURABLE PHASED ARRAY WITH p-i-n DIODES CONTROLLED 5

Fig. 4. Broadside radiation patterns with different d_3 at 31 GHz.

Fig. 6. Equivalent circuits of the directors and the dc feeding lines. (a) p-i-n diodes ON. (b) p-i-n diodes OFF.
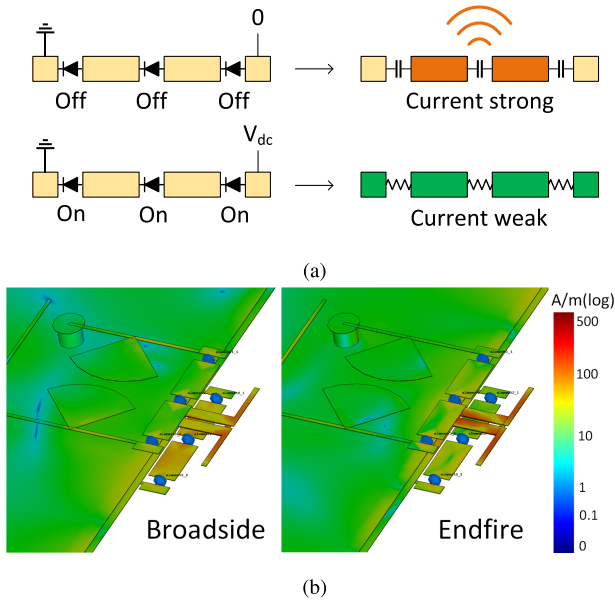

Fig. 5. Working principle. (a) Current magnitude with different p-i-n diodes state. (b) Surface current distribution of the broadside mode and the endfire mode at 28 GHz.

is 1 mm, while it shows much higher radiation in the endfire direction (90°) of the other two occasions.

The equivalent circuit of the proposed reconfigurable dipole antenna is shown in Fig. 3(b). The dipole is fed by an open-ended strip line through mutual coupling, and then, the dipole is coupled to two directors, where the coupling coefficients N_1 and N_2 depends on the state of the p-i-n diodes.

C. Realization of the Three Modes by Switching With mm-Wave p-i-n Diodes

The p-i-n diodes are utilized for switching the working modes. This section will first introduce the way of controlling the p-i-n diodes with dc supplies, and then, discuss the influence of parasitics on the antenna performance.

1) Mode Switching With mm-Wave p-i-n Diodes: The states of p-i-n diodes and the corresponding current distribution are shown in Fig. 5(a). The two ends of the strip are connected with dc feeding lines, as shown in Fig. 2(c). Due to the parasitic effect of p-i-n diodes at mm-wave frequencies, the two
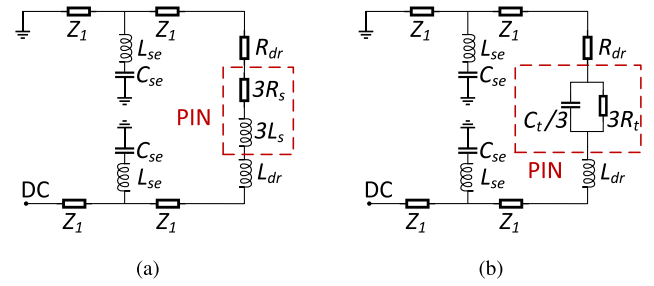
states will not be ideally ON and OFF. Here, we use capacitors to represent the OFF state and resistors to represent the ON state. The detailed discussion about parasitic effects will be shown in Section III-C2. When the p-i-n diodes are all OFF, the middle two parts are activated as directors, and strong current can be observed. As a result, the radiation direction is changed by the directors. The strip is not activated, when the p-i-n diodes are all "ON." Therefore, it has no influence on the radiation direction. The resonance of the long strip should be prevented because the strong current can cause high loss on the p-i-n diodes. In this design, the length of the long strip is tuned out of the operating band. By controlling the two strips independently, the dipole antenna will get four different radiation modes. With one strip activated and the other one not, the dipole antenna will have two different broadside radiation patterns. With both strips not activated, the dipole antenna will have the endfire radiation pattern. With both strips activated, the radiation pattern will be split into two broadside directions. The last mode is not adopted since it is covered by the other modes.

Fig. 5(b) is the surface current distribution of the broadside mode and the endfire mode at 28 GHz. For the endfire mode, both strips are not activated, and the current magnitude is low. For the broadside mode, the strip below is activated, but the one above is not. Relatively, the surface current on the strip below is much more significant than that on the strip above.

2) Parasitic Effect of p-i-n Diodes: The p-i-n diodes used in this design are MA4AGFCP910 from MACOM, and the data sheet is available in [29]. According to the data sheet, the working band is from 2 to 50 GHz. The equivalent circuits of the directors and dc feeding lines are shown in Fig. 6. The p-i-n diodes will be turned ON with forward dc current between 5 to 40 mA. The p-i-n diode in "ON" state can be modeled as the series of resistance $R_s = 5.2\,\Omega$ and inductance $L_s = 0.5$ nH, and in "OFF" state can be modeled as the parallel of capacitance $C_t = 0.021$ pF and resistance $R_t = 3 \times 10^5\,\Omega$. The maximum input power is $+23$ dBm and the operating temperature is from $+55\,°C$ to $-125\,°C$, which both fit the application scenarios of mobile terminals. For different types of p-i-n diodes, the parasitics are not the same; therefore, it is important to know which parameter has more influence on this antenna design.

1) *Resistance Loss of R_s:* The resistance loss is determined by two factors: the resistance and the through RF current. In our design, when the p-i-n diodes are in
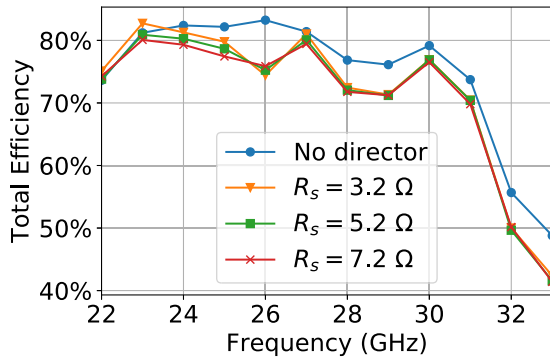
This article has been accepted for inclusion in a future issue of this journal. Content is final as presented, with the exception of pagination.

6

IEEE TRANSACTIONS ON MICROWAVE THEORY AND TECHNIQUES

Fig. 7.   Total efficiency of the endfire mode with different series resistance.
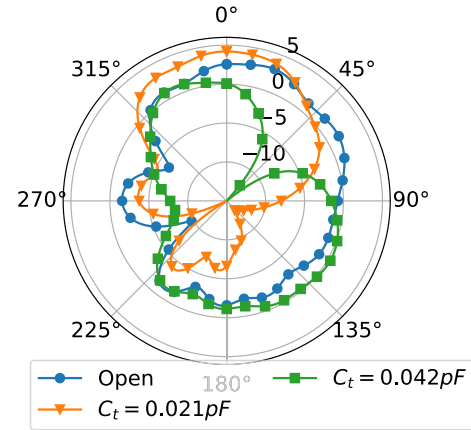

Fig. 8.   Broadside radiation patterns with different p-i-n diode parasitics at 28 GHz.

Fig. 9.   Simulated reflection coefficients of the proposed antenna.

the "ON" state, the whole strip is not resonant. In other words, the RF signal from the dipole antenna will not be coupled to this strip. Therefore, the magnitude of the RF through current is very low, and, as a result, the loss is much reduced. To verify this method, the endfire mode of the proposed antenna is simulated with the series resistance R_s ranging from 3.2 to 7.2 Ω. The endfire mode is chosen because all p-i-n diodes are in the "ON" state; therefore, it has the highest loss among the three working modes. The total efficiency is shown in Fig. 7. The blue line represents the efficiency of the dipole antenna without the directors. It also has the endfire radiation pattern but without the influence of p-i-n diodes. As we can see, the p-i-n diodes will bring an efficiency drop less than 10% (0.5 dB) over a wideband. If the p-i-n diodes are applied, the total efficiency shows no significant difference as the series resistance R_s ranging from 3.2 to 7.2 Ω. Because of the low through current in our design, the loss on the p-i-n diodes is much reduced, and the total efficiency will be much less impacted. This property makes the proposed antenna not sensitive to R_s, which is an advantage, especially for mm-wave antennas. The total efficiency will keep stable for different modes or even different p-i-n diodes.

2) *Capacitance C_t Influence:* When the p-i-n diodes are "OFF," the directors are resonant and the capacitance C_t also takes part in the resonance. The variation of C_t leads to the variation of resonant frequency, which changes the operating band of the antenna. Fig. 8 compares the radiation patterns with different values of C_t at 28 GHz. The radiation pattern without p-i-n diodes is also provided for comparison. The main beam direction is 0° when the value of C_t is 0.021 pF, which is from the datasheet. If the value of C_t is doubled (0.042 pF), the main beam direction turns to 335°. The radiation pattern without p-i-n diodes is very close to endfire, which has the main beam direction at 19°. The main beam direction or the operating band changing needs to be compensated by tuning the length of the directors, which is the separation between the p-i-n diodes. In practical commercial p-i-n diodes, the variation of C_t for the same type of p-i-n diodes is normally much smaller than the range in Fig. 8.
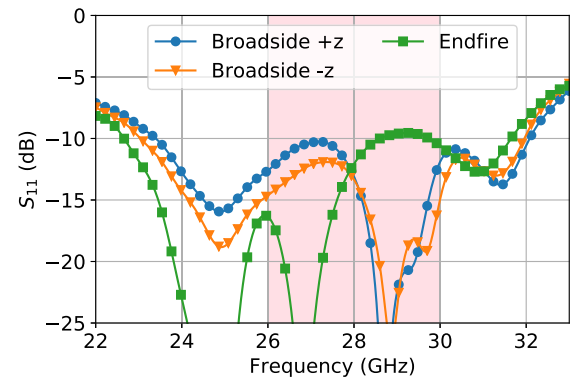
For instance, the C_t value of the p-i-n diode used in this design ranges from 0.018 to 0.021 pF. The broadside radiation pattern shows no significant difference in this range.

D. Simulated Antenna Element Performance

The simulated reflection coefficients are shown in Fig. 9. Since the current magnitude is always lower on the directors than those on the dipole, the impedance matching of the dipole is similar in different modes. All three modes have widely overlapped impedance matching band from 24 to 32 GHz. However, the main beam directions of the radiation patterns are determined by the resonant bandwidth of the directors. Therefore, the operating band in this article is defined by the performance of radiation patterns. In the operating band, the radiation patterns of the three modes are distinguishable, and, outside the operating band, the radiation patterns do not show too much difference. The operating band in the simulation is found out from 26 to 30 GHz with a relative bandwidth of 14.3%, which is marked as the pink area in Fig. 9.

The simulated H-plane (see *XOZ* plane in Fig. 2) radiation patterns in the operating band are shown in Fig. 10. The total efficiency in the simulation is between 75.9% and 81.3% for the broadside modes and between 70.8% to 81.3% for the endfire mode. As the frequency increases from 26 to 30 GHz, the electrical distance and position of the dipole
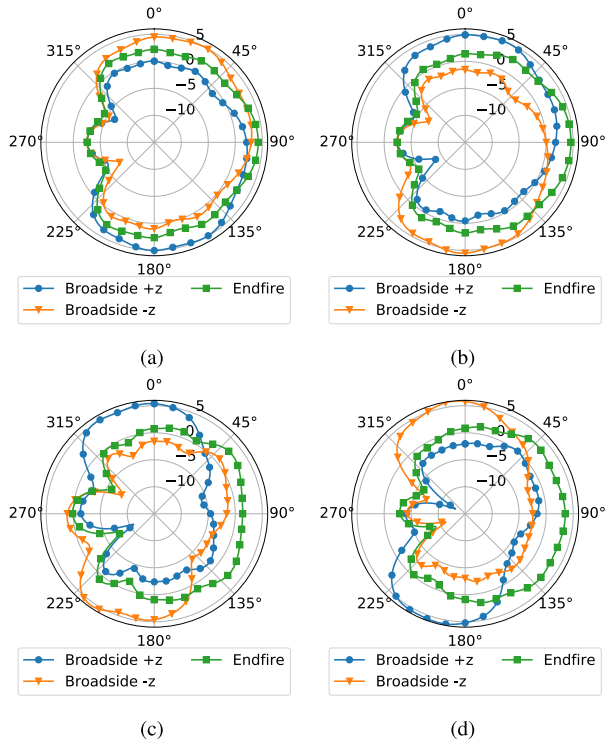
This article has been accepted for inclusion in a future issue of this journal. Content is final as presented, with the exception of pagination.

ZHANG *et al.*: RADIATION-PATTERN RECONFIGURABLE PHASED ARRAY WITH p-i-n DIODES CONTROLLED

7

Fig. 10.   Simulated *H*-plane (*XOZ* plane) radiation patterns of the proposed array element. (a) 26 GHz. (b) 27 GHz. (c) 29 GHz. (d) 30 GHz.

Fig. 11.   Simulated *E*-plane (*XOY* plane for endfire mode and *YOZ* plane for broadside modes) radiation patterns of the proposed array element. (a) Broadside +z. (b) Broadside −z. (c) Endfire.

and the directors are also changing, which leads to different gain and main beam directions across the operating band. In Fig. 10(a) and (b), the main beam directions of the two broadside modes are almost at 0° (Broadside +z) and 180° (Broadside −z) at 26 and 27 GHz, respectively. They tilt to 320° (broadside +z) and 220° (broadside −z) directions at 29 and 30 GHz, respectively, as shown in Fig. 10(c) and (d). The radiation patterns of the three modes become more distinguishable as the frequency increases, which also leads to the larger improvement of spatial coverage. The improvement at 26 GHz is still noteworthy to mention in the 3-D space, even though the peak gain differences from the 2-D radiation patterns are less than those in other frequencies. The discussion of the spatial coverage will be presented in Section III-E of array design. The simulated *E*-plane (see *XOY* plane for endfire mode and *YOZ* plane for the broadside modes in Fig. 2) radiation patterns in the operating band are shown in Fig. 11. Because of the different dielectric and the thickness of the material on the two sides of the dipole (Sub.3 on one side and Sub.1 and P1 on the other side), the radiation patterns of the two broadside modes are not exactly the same at the same operating frequency. The radiation patterns of the broadside −z mode in Fig. 11(b) is tilted to the +y-direction (150°) because the current distribution on the director is not balanced. The current on the +y-direction part is slightly stronger than that on the −y part.

E. Comparison With Dipole Backed With Conductor

In this section, the proposed antenna is compared with a dipole antenna backed with a conductor. The dipole backed with a conductor is shown in Fig. 12(a), where the dipole
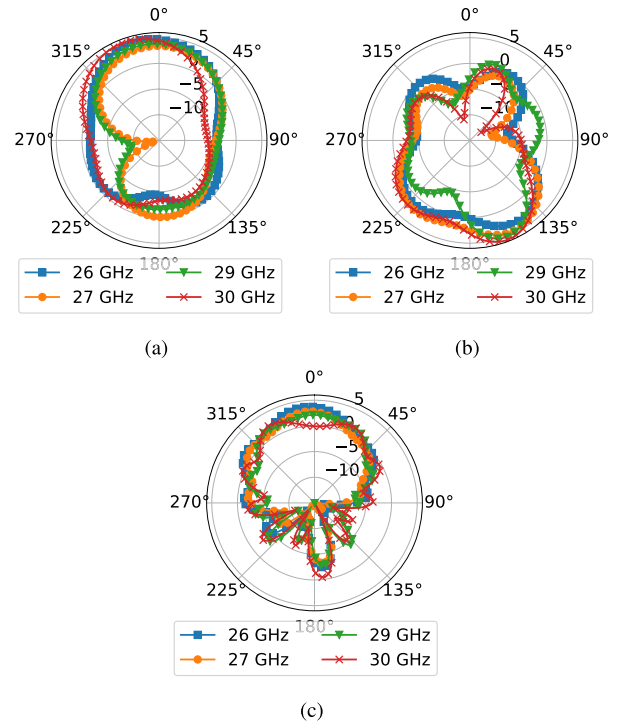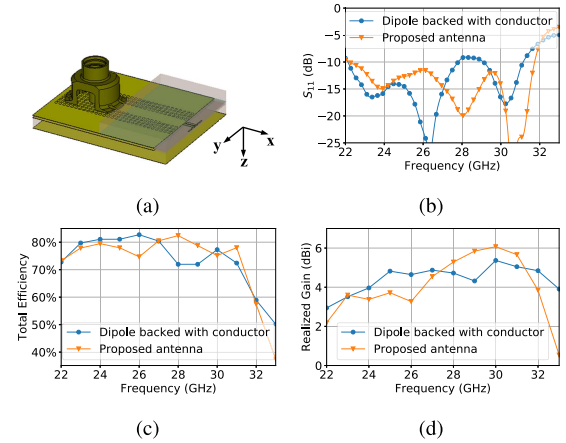

Fig. 12.   Dipole backed with conductor and simulation results comparing with the proposed reconfigurable antenna in the broadside −z mode. (a) Dipole back with conductor. (b) S_{11}. (c) Total efficiency. (d) Realized gain.

antenna and the feeding are the same as the proposed antenna. Since the dipole backed with conductor has only a broadside radiation pattern pointing at −z-direction, the comparison is made with the same mode of the proposed antenna.

The reflection coefficients are shown in Fig. 12(b). The proposed antenna has slightly better impedance matching and wider bandwidth than the dipole backed with a conductor. However, this result is reached with different profiles of the two antennas. The distance between the dipole to the conductor is 1.5 mm, while the distance between the dipole and the director layer is only 0.508 mm (h_1). The impedance matching will be deteriorated if the distance between the dipole to the conductor decreases to 0.508 mm. Therefore, the total profile

This article has been accepted for inclusion in a future issue of this journal. Content is final as presented, with the exception of pagination.

8   IEEE TRANSACTIONS ON MICROWAVE THEORY AND TECHNIQUES

of the dipole backed with conductor will be at least 2 mm higher than that of the proposed antenna, if another conductor is applied on the other side of the dipole in order to have two reconfigurable broadside radiation patterns pointing to either $+z$- or $-z$-direction. Considering the trend of the mobile handset is thinner and thinner, this 2 mm more thickness on antenna PCB will be a limitation to the whole profile of the handset.

In order to eliminate the influence of mismatching in the comparison of total efficiency and realized gain, the profile of the dipole with the conductor is also higher than the proposed antenna. The total efficiency of the two kinds of antennas is shown in Fig. 12(c). Both the proposed antenna and the dipole backed with conductor have efficiency of above 70% over a wideband. The dipole backed with conductor reaches the maximum efficiency at 26 GHz and the proposed antenna at 28 GHz in the simulation. The realized gain is shown in Fig. 12(d). The dipole backed with conductor has more stable gain over a wideband, while the proposed antenna has higher gain from 27 to 31 GHz than that at the other frequencies. The maximum gain of the proposed antenna is higher than the dipole backed with conductor.

In summary, if the antenna is realized by a dipole backed with conductor, the main performance degradation is the thickness. Moreover, this is an ideal case for the dipole backed with conductor. The way to reconfiguring the conductor, to arranging dc feeding, and the influence of the p-i-n diodes or switches are not considered in this model. In practice, all these following problems cannot be solved easily. While for the proposed antenna, it reaches a comparable performance with an ideal model and even with lower profile. The influence of the dc feeding and p-i-n diodes is reduced to a very low level, which is a big challenge for the mm-wave reconfigurable antenna design.

IV. DESIGN OF FOUR-ELEMENT ARRAY

In this section, the design of a four-element array constructed by the proposed reconfigurable array elements is introduced. It includes the following parts: 1) the array structure and S-parameter measurements; 2) the radiation pattern measurements; and 3) the performance of beam scanning and spatial coverage.

A. Array Structure and S-Parameter Measurements

The proposed array is fabricated, as shown in Fig. 13. The interelement distance is 5.5 mm ($0.5\lambda_0$) at 28 GHz. The right ends of the directors are grounded. The left ends are connected to a common dc feeding line through an 18-nH inductor. Another 18-nH inductor and a 50-Ω resistor are connected to the common dc feeding line. The inductors and resistors are included in the dc feeding network. The use of inductors is for facilitating the manually soldered p-i-n diodes of each element, and they can be replaced by transmission lines in practice. The resistors are utilized for limiting the dc current as a protection of the p-i-n diodes. In the massive production, this function will be provided by DSP. The inductors and resistors work at

TABLE II
DC SUPPLY AND P-I-N DIODES STATUS
FOR DIFFERENT WORKING MODES

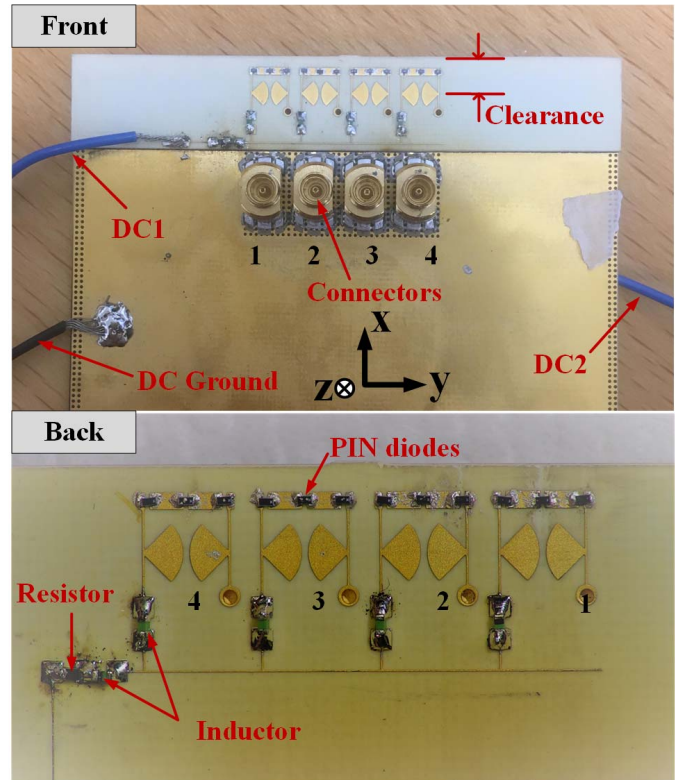|	DC1	DC2
Broadside +z	V_{dc}	0
Broadside -z	0	V_{dc}
Endfire	V_{dc}	V_{dc}

Fig. 13.   Structure of the proposed four-element array.

the low frequencies and due to the presence of RF chocks, and they have no impact on the antenna performance.

The p-i-n diodes are mounted on the directors with high-frequency conductive glue (where the performance is very similar to silver). All the p-i-n diodes on the same side are in the same "ON" or "OFF" state. The p-i-n diodes on the front side (see M5 layer in Fig. 2) are controlled by DC1, and on the backside (M1) are controlled by DC2. Both dc feedings share the same ground with the RF signal. A dc current of 20 mA is applied when the state is "ON" and dc voltage is 0 V when the state is "OFF." The dc supply states corresponding to the array working modes are summarized in Table II. To be noticed, the value of V_{dc} is set to fulfill the requirement of through dc current on the p-i-n diodes. It will be controlled by a current limiting resistor, as shown in Fig. 13. The value of V_{dc} and the current limiting resistor can be set according to the power supply in practice.

The simulated and measured S-parameters are shown in Fig. 14. Fig. 14(a) and (b) are the reflection coefficients of array element 3 and 4, respectively. It should be noticed that the operating band of the proposed antenna is also
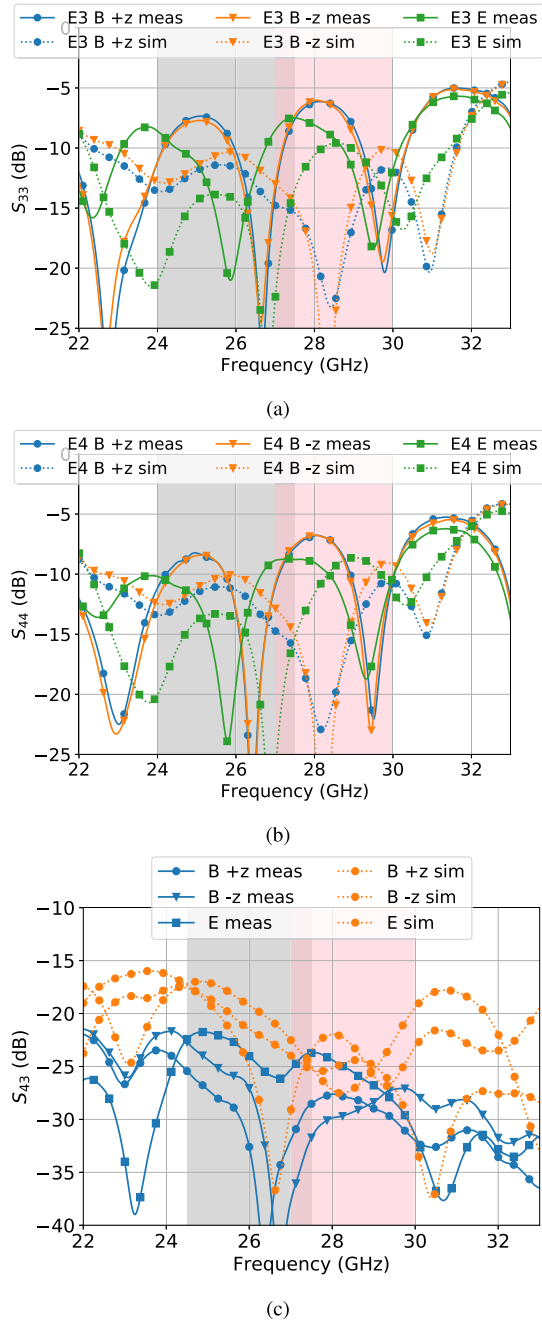
This article has been accepted for inclusion in a future issue of this journal. Content is final as presented, with the exception of pagination.

ZHANG *et al.*: RADIATION-PATTERN RECONFIGURABLE PHASED ARRAY WITH p-i-n DIODES CONTROLLED

9

Fig. 14. Simulated and measured S-parameters of array element 3 and 4. (a) Reflection coefficients of array element 3. (b) Reflection coefficients of array element 4. (c) Mutual coupling of array element 3 and 4.
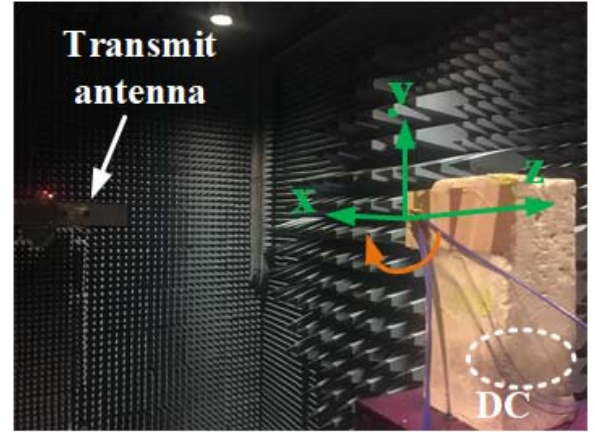

Fig. 15. Setup of the radiation pattern measurement.

within the corresponding simulated and measured operating bands. The array element 1 and 2 have similar results as the array element 3 and 4. The results of the array elements are very similar to those of a single antenna in the corresponding operating band, as shown in Fig. 9. It also proves the low interference between the array elements.

B. Radiation Pattern Measurements

The proposed array is mounted on a 60 mm × 130 mm ground plane, which is close to the size of a mobile phone and measured in an anechoic chamber. Fig. 15 shows the setup in the measurements. The transmitting antenna is fixed, and the proposed array is the receiving antenna. The array-under-test is installed on a rotational axis, and the array center is at the rotating center. The radiation patterns of all the array elements and all the modes are measured, but only the results of the middle/embedded array element (element 3) are presented. Due to the operating frequency shift, the comparison between the simulations and the measurements is made with a 3-GHz frequency shift. For instance, the measured 24-GHz radiation patterns are compared with the simulated 27-GHz corresponding radiation patterns. The reason for this frequency shifting will be discussed in Section V-A with postsimulations and comparisons. The simulated and measured H-plane (see *XOZ* plane in Fig. 2 or Fig. 15) radiation patterns of the array element 3 are shown in Fig. 16. As we can see, the simulations and measurements have a good match. A null is observed in the broadside $-z$ measured radiation patterns at 270° for all the frequencies, which may come from the influence of the testing cable. The simulated and measured E-plane (see *XOY* plane for endfire mode and *YOZ* plane for the broadside modes in Fig. 2 or Fig. 15) radiation patterns are shown in Fig. 17. Comparing with the single antenna simulations in Fig. 11, many ripples are observed in the array radiation patterns. The reason is that the array pattern is simulated and measured on an electric large-ground plane, which supports the propagation and radiation of the surface wave along the y-axis direction.

Fig. 18 shows the realized gain and total efficiency in the simulations and measurements when all the array elements are in phase. The dash-dot lines represent the realized gain in the simulation from 26 to 30 GHz. The two broadside modes

defined by the performance of radiation patterns. An operating frequency shift is observed in the radiation pattern simulations and measurements due to the conductive glue thickness. The details will be explained in Section V-A. The gray area represents the measured operating band of 24–27.5 GHz, while the pink area is the simulated band of 26–30 GHz. The simulated and measured relative bandwidth is 14.3% and 13.4%, respectively. The measurements are slightly mismatched in the operating band, which is also due to the influence of the conductive glue thickness, but the reflection is still lower than -7.5 dB. Fig. 14(c) is the mutual coupling between array element 3 and 4. The coupling is similar and below -20 dB

This article has been accepted for inclusion in a future issue of this journal. Content is final as presented, with the exception of pagination.

10   IEEE TRANSACTIONS ON MICROWAVE THEORY AND TECHNIQUES
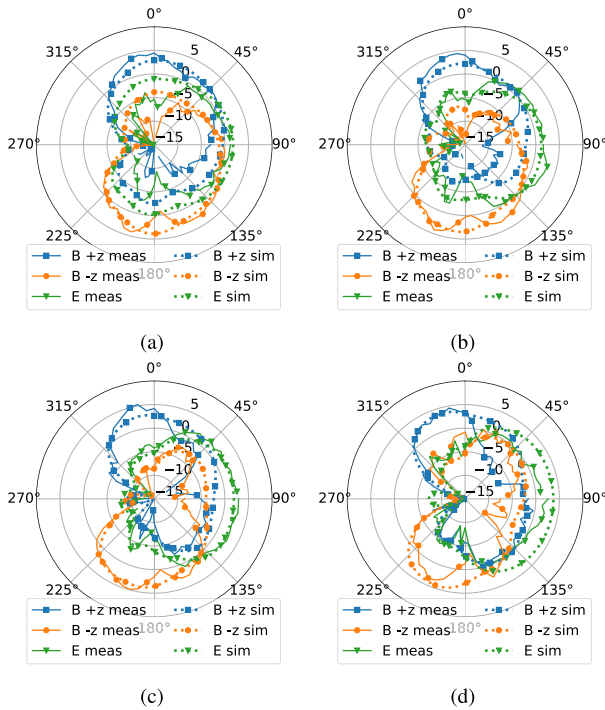
Fig. 16. Simulated and measured *H*-plane (*XOZ* plane) radiation patterns of array element 3. (a) Simulated 27 GHZ and measured 24 GHz. (b) Simulated 28 GHz and measured 25 GHz. (c) Simulated 29 GHz and measured 26 GHz. (d) Simulated 30 GHz and measured 27 GHz.

Fig. 17. Simulated and measured *E*-plane (*YOZ* plane for the broadside modes and *XOY* plane for the endfire modes) radiation patterns of array element 3 in the operating band. (a) Simulated 27 GHZ and measured 24 GHz. (b) Simulated 28 GHz and measured 25 GHz. (c) Simulated 29 GHz and measured 26 GHz. (d) Simulated 30 GHz and measured 27 GHz.
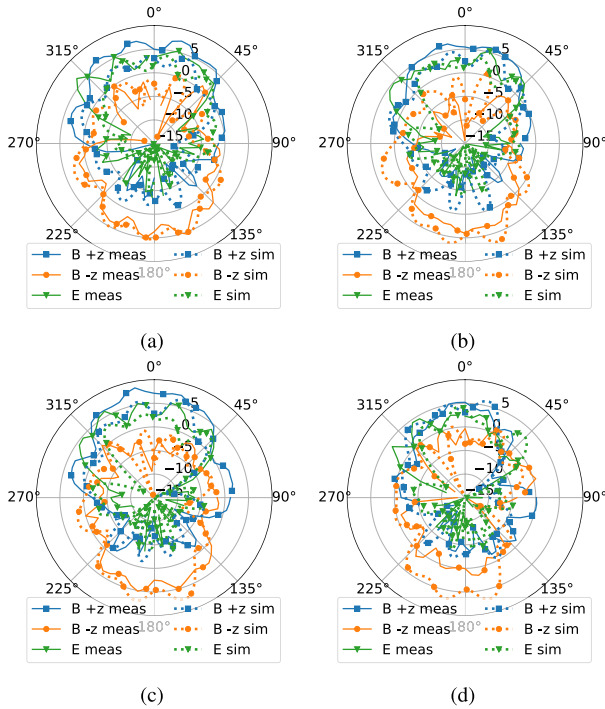
have a difference around 0.5 dB because of the substrates differences on the two sides of the dipole. The gain of endfire modes is lower than the broadside modes due to
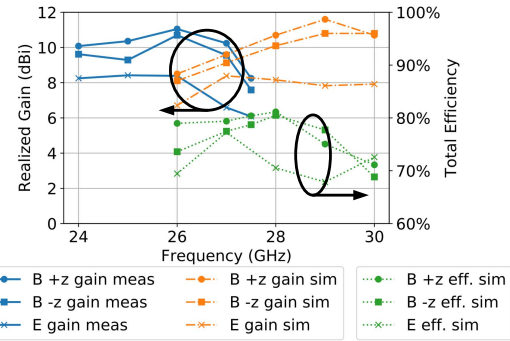

Fig. 18. Simulated and measured realized gain and simulated total efficiency of the proposed array when all the array elements are in phase.

wider beamwidth. The gain of the three modes increased from 26 to 29 GHz and decreases from 29 to 30 GHz, which indicates the effects of the directors. The highest gain achieves when the directors operate close to their resonant frequencies. The solid lines represent the realized gain in the measurements from 24 to 27.5 GHz. The measurement results follow the same trend as the simulations. The two broadside modes have a similar gain difference to the simulations and the gain of broadside $+z$ mode is still higher than that of broadside $-z$ mode. The gain of endfire mode is lower compared with both broadside modes. The gain of the three modes increases from 24 to 26 GHz and decreases from 26 to 27.5 GHz, which indicates that the resonant frequency of the directors moves to a lower frequency compared with the simulation. The total efficiency in the simulations is shown as the dot lines. The endfire mode has lower efficiency than the broadside modes because the p-i-n diodes are all ON, and thus, the total parasitic resistance is higher. All three modes have total efficiency between 68% to 80%. Since the realized gain level in the measurements is very close to the simulation, it is reasonable to believe that the total efficiency in the measurements is also similar to the simulations.

C. Beam Scanning and Spatial Coverage

The beam scanning and spatial coverage are investigated in the simulation. The E-plane beam scanning of the three modes at 28 GHz is shown in Fig. 19(a)–(c). For each mode, nine beams are adopted to demonstrate the scanning range. The scanning angle is from $-50°$ to $50°$ for the two broadside modes and from $-40°$ to $40°$ for the endfire mode. The realized gain is from 7 to 10 dBi for broadside $+z$ mode, 8.5 to 10.7 dBi for broadside $-z$ mode, and 5.3 to 8.2 dBi for the endfire mode. The active reflection coefficients (ARCs) of array element 3 is shown in Fig. 19(d). The angles 0° and 150° are the feeding phase difference, which corresponds to the array elements in phase and with the largest scanning angle. The ARC is below -10 dB when in-phase and below -6 dB when scanning at largest angle, which is still under an acceptable level.

The spatial coverage of the proposed array is shown in Fig. 20. For each frequency, it is calculated by the highest achievable gain at each direction of the 3-D space from all the possible beams generated by the beam switching

This article has been accepted for inclusion in a future issue of this journal. Content is final as presented, with the exception of pagination.

ZHANG *et al.*: RADIATION-PATTERN RECONFIGURABLE PHASED ARRAY WITH p-i-n DIODES CONTROLLED

11

TABLE III
COMPARISON WITH DIFFERENT 5G mm-WAVE ANTENNAS FOR HANDSETS

Ref No.	Operating Band (GHz)	Dimensions* (mm^2)	Number of Array Elements	Spatial Coverage at 5 dBi	Reconfigurable
[5]	21-22	3.787 × 4.5	24	Not given	No
[6]	26-28	10.5 × 0.5	24	87%	No
[30]	27.2-28.2	1 × 7.1	16	Not given	No
[31]	27.5-30	1.5 × 4	16	Not given	No
[7]	27.5-28.5	7.8 × 2.508	8	65%	Yes
[32]	25-33	2.1 × 1.724	8	50%	No
This work	24-27.5	4 × 1.391	4	80%	Yes

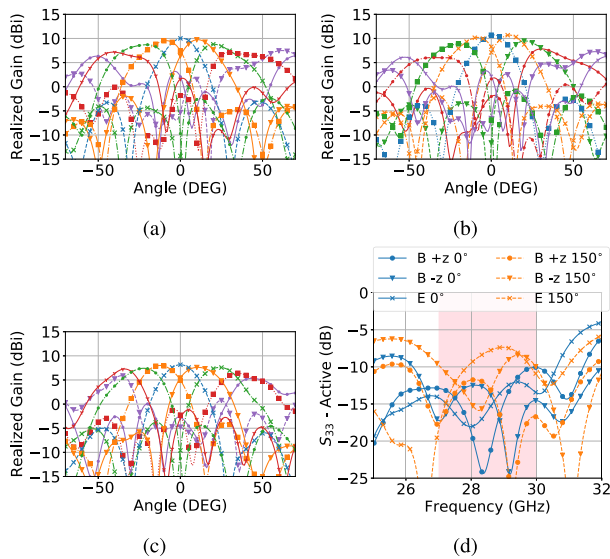Dimensions*: the first component represents the clearance; the second component represents the thickness.

Fig. 19. Simulated beam scanning *E*-plane patterns at 28 GHz and ARCs of array element 3. (a) Broadside +*z*. (b) Broadside −*z*. (c) Endfire. (d) ARCs of array element 3.
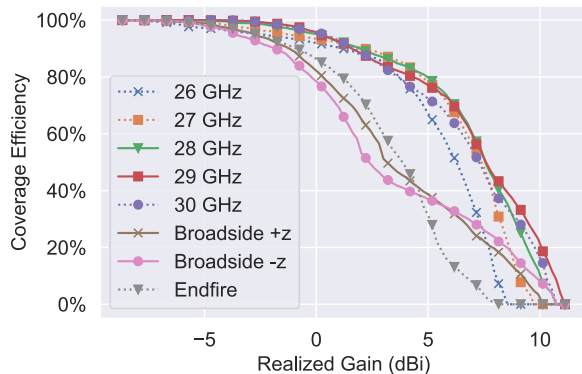

Fig. 20. Coverage efficiency of the proposed array.

and beam scanning. According to the UE spherical coverage for power class 2 in 3GPP specification [27], the minimum EIRP at 60% CDF is 18 dBm for frequency band n258 (24.25–27.50 GHz). If we consider the transmission power of 20 mW (13 dBm), the antenna gain should be at least 5 dBi for the corresponding coverage. The "broadside +*z*," "broadside −*z*," and "endfire" represent the coverage efficiency of each single-mode at 28 GHz. The array can cover

more than 90% space at 0-dBi gain in the whole operating band. At realized gain at 5 dBi, the coverage efficiency at 26 GHz is around 65%, at 30 GHz is around 70%, and at all the other frequencies is around 80%. For only one working mode, which represents the arrays without beam switching, the coverage efficiency at 5-dBi gain is from 30% to 40%.

As mentioned in Section III-E, the proposed beam switching antenna reaches nearly the same total efficiency and bandwidth as a dipole antenna backed with a large reflector, while the proposed antenna has a much lower profile. The performance of the proposed array is also compared with two dipole arrays backed with conductors on different sides. The profile of the dipole arrays with conductor is higher in order to reach the same impedance matching as the proposed array. The total efficiency is similar in both cases. The coverage efficiency of the array with conductor is slightly lower than the proposed array. Furthermore, the switching loss between two reflector-backed dipoles is not considered here, but the p-i-n diode loss in the proposed array is included. The loss of a commercial switch module in mm-wave bands is at least 2 dB currently.

In Table III, the performance of the proposed antenna is compared with some other 5G mm-wave antennas for handset devices. The first element of the dimensions represents the clearance, and the second is the thickness of the PCB. The works in [5] and [6] are reported in the introduction as examples of beam switching arrays, which contain three subarrays. In [30] and [31], the arrays are integrated with the metallic casing of the phone, which reduces the clearance but increases the thickness. Two subarrays, which contain eight array elements each, are implemented to improve the spatial coverage. The work in [7] is also mentioned in the introduction due to the reconfiguration of the radiation pattern of the array elements. The array in [32] is presented as a wide scan angle array to achieve high spatial coverage over a wideband. Compared with all those articles, the proposed array has the least array elements but still reach the same and higher spatial coverage than [7] and [32]. It also has higher bandwidth and smaller dimensions than [5]–[7].

V. REALISTIC OPERATING ENVIRONMENT IMPACT

In this section, some impacts from the realistic operating environment are discussed. First, the influence of the solder paste for the p-i-n diodes is presented, and then the array performance in a real mobile phone model is introduced.

This article has been accepted for inclusion in a future issue of this journal. Content is final as presented, with the exception of pagination.

12   IEEE TRANSACTIONS ON MICROWAVE THEORY AND TECHNIQUES
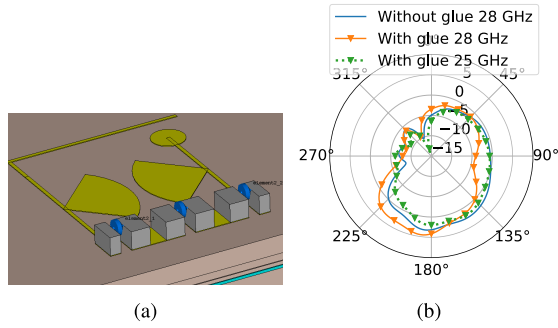

Fig. 21.   Influence of the conductive glue. (a) Antenna model with conductive glue. (b) Radiation patterns with conductive glue.
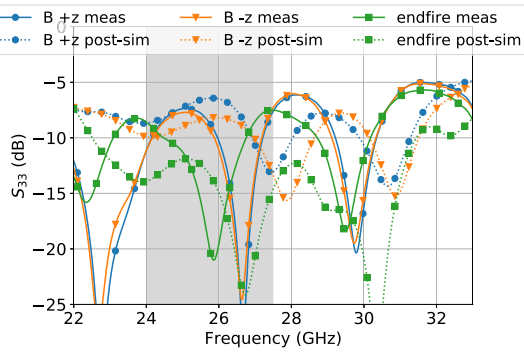

Fig. 22.   Postsimulated and measured reflection coefficients of array element 3.

Fig. 23.   Postsimulated and measured H-plane (XOZ plane) radiation patterns of array element 3 with conductive glue in the simulations. (a) 24 GHz. (b) 25 GHz. (c) 26 GHz. (d) 27 GHz.

Fig. 24.   Postsimulated and measured E-plane (YOZ plane for the broadside modes and XOY plane for the endfire modes) radiation patterns of array element 3 with conductive glue in the operating band. (a) 24 GHz. (b) 25 GHz. (c) 26 GHz. (d) 27 GHz.

A. Influence of Solder Paste

In the measurement, the p-i-n diodes are soldered manually with conductive glue, whose main ingredient is silver. Therefore, the position, amount, and distribution of the conductive glue cannot be controlled very well. The conductive glue introduces parasitics into the directors and, as a result, changes their resonant frequency. In this section, the influence of the conductive glue is investigated, and the comparison between the measured array and the postsimulated model with conductive glue is provided.

Fig. 21(a) shows a model of the proposed antenna with conductive glue on the directors. The conductive glue is silver and has a height of 0.5 mm. The simulated H-plane (XOZ) radiation patterns of broadside $-z$ mode is shown in Fig. 21(b). At the same frequency of 28 GHz, the radiation pattern of the antenna with conductive glue has a null at the endfire direction (90°) and higher gain at the broadside direction comparing to the antenna without conductive glue. This is because the conductive glue makes the operating band shifting to lower frequencies. As we can see, the radiation pattern of the proposed antenna without the conductive glue at 28 GHz is similar to those of the antenna with conductive glue at 25 GHz. As a conclusion of this experiment, 0.5-mm-thick conductive glue is able to move the operating band by around 3-GHz lower.

Comparisons between the measurements and postsimulations are presented. A 0.5-mm-thick conductive glue is added to all the directors in the postsimulations of the proposed array. The reflection coefficients are shown in Fig. 22. The gray area marks the operating band from 24 to 27.5 GHz.
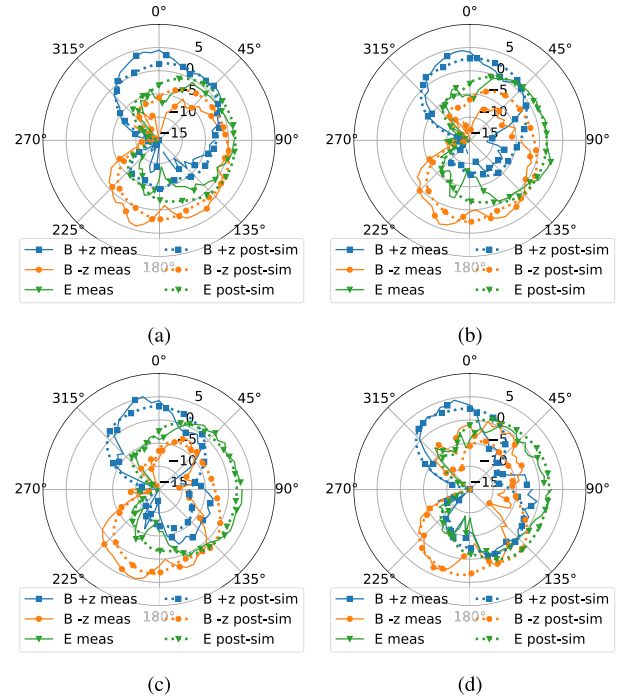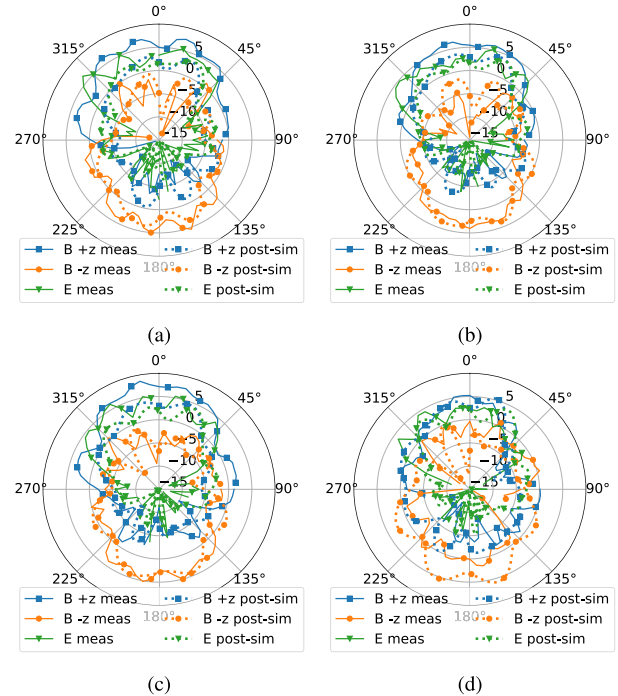
The postsimulations are slightly mismatched, and the results agree with the measurements. By slightly tuning some parameters ($l_a = 3.8$ mm, $h_a = 1.3$ mm, $S_a = 0.2$ mm, and $W_s = 0.6$ mm), a -10-dB reflection can be reached. In the massive production, the influence of p-i-n diodes can be much
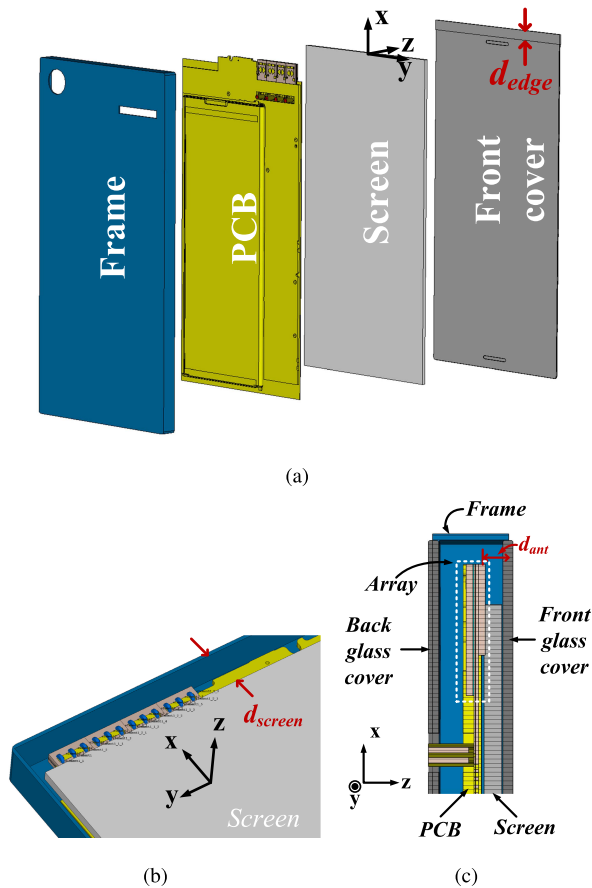
(a)

(b)

Fig. 25. Configuration of the proposed array in a mobile phone model. (a) Explored view. (b) View of the proposed array. (c) Side view.

(a)   (b)

Fig. 26. Radiation patterns of the broadside $+z$ mode with the mobile phone model. (a) Patterns with different d_{edge}. (b) Patterns with different d_{ant}.

minimized by precisely controlled soldering procedures. The coupling does not show too much difference after adding the conductive glue in the simulations.

The simulated and measured H-plane (XOZ) radiation patterns of the three modes from 24 to 27 GHz are shown in Fig. 23. As we can see, considering the conductive glue, the simulations and measurements have reached a good agreement. Fig. 24 shows the simulated and measured E-plane (YOZ plane for the broadside modes and XOY plane for the endfire modes) radiation patterns with conductive glue in the simulation model. The gain differences are caused by the different tilting of the beams.

B. Array Performance in Mobile Phone Model

The proposed array is simulated in a real mobile phone model, as shown in Fig. 25(a), which includes a screen ($\epsilon_r = 4.82$ and $\tan\delta = 0.0054$), a plastic frame ($\epsilon_r = 3$), a PCB board (modeled as copper), and a glass front cover ($\epsilon_r = 6.84$ and $\tan\delta = 0.0297$). The proposed array is mounted in the corner of the PCB board, as shown in Fig. 25(b). The dc feedings of the proposed array are touched with the screen. The distance between the top edge of the screen to the plastic frame is $d_{\mathrm{screen}} = 4.95$ mm ($0.46\lambda_0$ at 28 GHz). Each part of the phone model has a different level of influence on antenna performance. The plastic frame has no significant influence due to the low dielectric constant. The screen
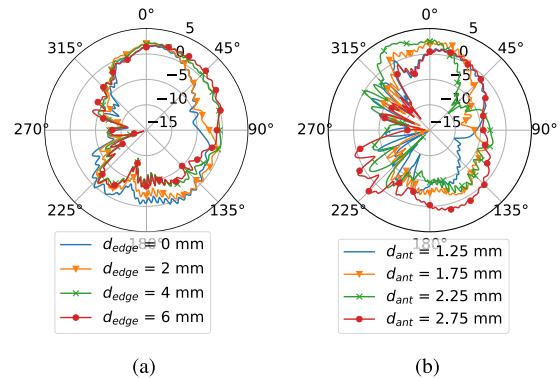
will not have significant influence if the radiating parts fit in the 4.95-mm gap. The glass front cover does not have significant influence on the endfire radiation but has a strong reflection of the broadside radiation due to the high dielectric constant.

Two possible methods can solve this problem. One is to add a plastic edge on the top of the glass cover in order to reduce the reflection above the array. Fig. 26(a) shows the radiation patterns of the broadside $+z$ mode of array element 3 with different width of the edge (d_{edge}). As we can see, by increasing the width of the gap, the front to back ratio and the realized gain increase. The improvement from $d_{\mathrm{edge}} = 4$ mm ($0.37\lambda_0$ at 28 GHz) to $d_{\mathrm{edge}} = 6$ mm ($0.56\lambda_0$ at 28 GHz) is not very significant; therefore, further increasing the width of the edge will not bring more benefits.

Another solution is to add an identical glass cover on the back of the phone in order to cancel out the reflection from the front cover. In this case, the distance between the antenna and the glass layers (d_{ant}) needs to be tuned in order to reach best cancellation. Fig. 26(b) shows the radiation patterns of the broadside $+z$ mode with different d_{ant}. As we can see, the best broadside gain is reached when d_{ant} is 2.25 mm ($0.21\lambda_0$ at 28 GHz) for broadside $+z$ mode. The two solutions are only two possibilities to this example model and are practical in real designs. There could also be some other solutions depending on the detailed phone configurations.

VI. CONCLUSION

This article has presented a four-element phased array with radiation pattern-reconfigurable array elements for 5G mobile terminal applications. The proposed array is designed for a hybrid antenna system, which reaches large spatial coverage but contains much fewer components compared with the conventional multiarray system. The operating band is from 24 to 27.5 GHz in the measurement, which covers the allocated 5G band for Europe. The beam switching is simple, stable, and not sensitive to the resistance loss of p-i-n diodes, which guarantees high total efficiency. The array, which has been fabricated by multilayer substrate, has a low profile and planer structure. The small required clearance makes the array easily integrated into most of the current mobile phones. All the properties have shown that the proposed antenna and array are good candidates for the 5G terminals.

REFERENCES

[1] W. Hong, K.-H. Baek, and S. Ko, "Millimeter-wave 5G antennas for smartphones: Overview and experimental demonstration," *IEEE Trans. Antennas Propag.*, vol. 65, no. 12, pp. 6250–6261, Dec. 2017.

[2] T. S. Rappaport *et al.*, "Millimeter wave mobile communications for 5G cellular: It will work!" *IEEE Access*, vol. 1, pp. 335–349, 2013.

[3] M. K. Samimi and T. S. Rappaport, "3-D millimeter-wave statistical channel model for 5G wireless system design," *IEEE Trans. Microw. Theory Techn.*, vol. 64, no. 7, pp. 2207–2225, Jul. 2016.

[4] J. Helander, K. Zhao, Z. Ying, and D. Sjöberg, "Performance analysis of millimeter-wave phased array antennas in cellular handsets," *IEEE Antennas Wireless Propag. Lett.*, vol. 15, pp. 504–507, Mar. 2016.

[5] N. Ojaroudiparchin, M. Shen, S. Zhang, and G. F. Pedersen, "A switchable 3-D-coverage-phased array antenna package for 5G mobile terminals," *IEEE Antennas Wireless Propag. Lett.*, vol. 15, pp. 1747–1750, 2016.

[6] S. Zhang, X. Chen, I. Syrytsin, and G. F. Pedersen, "A planar switchable 3-D-coverage phased array antenna and its user effects for 28-GHz mobile terminal applications," *IEEE Trans. Antennas Propag.*, vol. 65, no. 12, pp. 6413–6421, Dec. 2017.

[7] J. Zhang, S. Zhang, X. Lin, Y. Fan, and G. F. Pedersen, "3D radiation pattern reconfigurable phased array for transmission angle sensing in 5G mobile communication," *Sensors*, vol. 18, no. 12, p. 4204, 2018. [Online]. Available: http://www.mdpi.com/1424-8220/18/12/4204

[8] J. Y. Lau and S. V. Hum, "A planar reconfigurable aperture with lens and reflectarray modes of operation," *IEEE Trans. Microw. Theory Techn.*, vol. 58, no. 12, pp. 3547–3555, Dec. 2010.

[9] H. Li *et al.*, "Reconfigurable diffractive antenna based on switchable electrically induced transparency," *IEEE Trans. Microw. Theory Techn.*, vol. 63, no. 3, pp. 925–936, Mar. 2015.

[10] P.-Y. Qin, Y. J. Guo, and C. Ding, "A beam switching quasi-Yagi dipole antenna," *IEEE Trans. Antennas Propag.*, vol. 61, no. 10, pp. 4891–4899, Oct. 2013.

[11] H. Li, B. K. Lau, and S. He, "Design of closely packed pattern reconfigurable antenna array for MIMO terminals," *IEEE Trans. Antennas Propag.*, vol. 65, no. 9, pp. 4891–4896, Sep. 2017.

[12] F. A. Dicandia, S. Genovesi, and A. Monorchio, "Efficient excitation of characteristic modes for radiation pattern control by using a novel balanced inductive coupling element," *IEEE Trans. Antennas Propag.*, vol. 66, no. 3, pp. 1102–1113, Mar. 2018.

[13] A. Pal, A. Mehta, D. Mirshekar-Syahkal, and H. Nakano, "A twelve-beam steering low-profile patch antenna with shorting vias for vehicular applications," *IEEE Trans. Antennas Propag.*, vol. 65, no. 8, pp. 3905–3912, Aug. 2017.

[14] M. S. Alam and A. M. Abbosh, "Wideband pattern-reconfigurable antenna using pair of radial radiators on truncated ground with switchable director and reflector," *IEEE Antennas Wireless Propag. Lett.*, vol. 16, pp. 24–28, 2017.

[15] H.-W. Deng, T. Xu, and F. Liu, "Broadband pattern-reconfigurable filtering microstrip antenna with quasi-Yagi structure," *IEEE Antennas Wireless Propag. Lett.*, vol. 17, no. 7, pp. 1127–1131, Jul. 2018.

[16] S.-L. Chen, P.-Y. Qin, W. Lin, and Y. J. Guo, "Pattern-reconfigurable antenna with five switchable beams in elevation plane," *IEEE Antennas Wireless Propag. Lett.*, vol. 17, no. 3, pp. 454–457, Mar. 2018.

[17] S.-L. Chen, P.-Y. Qin, C. Ding, and Y. J. Guo, "Cavity-backed proximity-coupled reconfigurable microstrip antenna with agile polarizations and steerable beams," *IEEE Trans. Antennas Propag.*, vol. 65, no. 10, pp. 5553–5558, Oct. 2017.

[18] Y. Yashchyshyn, J. Marczewski, and D. Tomaszewski, "Investigation of the S-PIN diodes for silicon monolithic antennas with reconfigurable aperture," *IEEE Trans. Microw. Theory Techn.*, vol. 58, no. 5, pp. 1100–1106, May 2010.

[19] C.-C. Cheng, B. Lakshminarayanan, and A. Abbaspour-Tamijani, "A programmable lens-array antenna with monolithically integrated MEMS switches," *IEEE Trans. Microw. Theory Techn.*, vol. 57, no. 8, pp. 1874–1884, Aug. 2009.

[20] P. Sanchez-Olivares and J. L. Masa-Campos, "Mechanically reconfigurable conformal array antenna fed by radial waveguide divider with tuning screws," *IEEE Trans. Antennas Propag.*, vol. 65, no. 9, pp. 4886–4890, Sep. 2017.

[21] I. F. da Costa, A. Cerqueira S., Jr., D. H. Spadoti, L. G. da Silva, J. A. J. Ribeiro, and S. E. Barbin, "Optically controlled reconfigurable antenna array for mm-wave applications," *IEEE Antennas Wireless Propag. Lett.*, vol. 16, pp. 2142–2145, May 2017.

[22] C. T. Rodenbeck, M.-Y. Li, and K. Chang, "Circular-polarized reconfigurable grating antenna for low-cost millimeter-wave beam-steering," *IEEE Trans. Antennas Propag.*, vol. 52, no. 10, pp. 2759–2764, Oct. 2004.

[23] Y. Yashchyshyn, K. Derzakowski, P. R. Bajurko, J. Marczewski, and S. Kozlowski, "Time-modulated reconfigurable antenna based on integrated S-PIN diodes for mm-wave communication systems," *IEEE Trans. Antennas Propag.*, vol. 63, no. 9, pp. 4121–4131, Sep. 2015.

[24] A. Clemente, L. Dussopt, R. Sauleau, P. Potier, and P. Pouliguen, "1-bit reconfigurable unit cell based on pin diodes for transmit-array applications in *X*-band," *IEEE Trans. Antennas Propag.*, vol. 60, no. 5, pp. 2260–2269, May 2012.

[25] L. Di Palma, A. Clemente, L. Dussopt, R. Sauleau, P. Potier, and P. Pouliguen, "1-bit reconfigurable unit cell for Ka-band transmitarrays," *IEEE Antennas Wireless Propag. Lett*, vol. 15, pp. 560–563, 2016.

[26] L. Di Palma, A. Clemente, L. Dussopt, R. Sauleau, P. Potier, and P. Pouliguen, "Circularly-polarized reconfigurable transmitarray in Ka-band with beam scanning and polarization switching capabilities," *IEEE Trans. Antennas Propag.*, vol. 65, no. 2, pp. 529–540, Feb. 2017.

[27] *User Equipment (UE) Radio Transmission and Reception; Part 2: Range 2 Standalone (Release 15)*, document TS38.101-2 v15.4.0, Jan. 2019.

[28] H. Aliakbari, A. Abdipour, A. Costanzo, D. Masotti, R. Mirzavand, and P. Mousavi, "Far-field-based nonlinear optimization of millimeter-wave active antenna for 5G services," *IEEE Trans. Microw. Theory Techn.*, vol. 67, no. 7, pp. 2985–2997, Jul. 2019.

[29] *Aluminum Gallium Arsenide Flip Chip Pin Diodes*. [Online]. Available: https://www.macom.com/products/product-detail/MADP-001907-13050P

[30] J. Bang and J. Choi, "A SAR reduced mm-wave beam-steerable array antenna with dual-mode operation for fully metal-covered 5G cellular handsets," *IEEE Antennas Wireless Propag. Lett.*, vol. 17, no. 6, pp. 1118–1122, Jun. 2018.

[31] B. Yu, K. Yang, C.-Y.-D. Sim, and G. Yang, "A novel 28 GHz beam steering array for 5G mobile device with metallic casing application," *IEEE Trans. Antennas Propag.*, vol. 66, no. 1, pp. 462–466, Jan. 2018.

[32] I. Syrytsin, S. Zhang, G. F. Pedersen, and A. S. Morris, "Compact quad-mode planar phased array with wideband for 5G mobile terminals," *IEEE Trans. Antennas Propag.*, vol. 66, no. 9, pp. 4648–4657, Sep. 2018.

Jin Zhang was born in Anshun, Guizhou, China, in 1989. She received the B.E. degree from the University of Electronic Science and Technology of China, Chengdu, China, in 2012. She is currently pursuing the Ph.D. degree in reconfigurable antenna design for the next generation of mobile terminals at Aalborg University, Aalborg, Denmark.

Her current research interests include mm-wave antenna design for mobile terminals, reconfigurable, and dual- and circular-polarization antenna design.
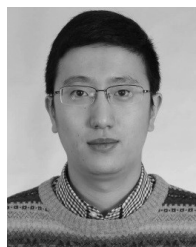
Shuai Zhang (SM'18) received the B.E. degree from the University of Electronic Science and Technology of China, Chengdu, China, in 2007, and the Ph.D. degree in electromagnetic engineering from the KTH Royal Institute of Technology (KTH), Stockholm, Sweden, in 2013.

He was a Research Fellow at KTH. In 2010 and 2011, he was a Visiting Researcher with Lund University, Lund, Sweden, and Sony Mobile Communications AB, Lund, respectively. In 2014, he joined Aalborg University, Aalborg, Denmark, where he is currently an Associate Professor. He was also an external antenna specialist at Bang & Olufsen, Struer, Denmark, from 2016 to 2017. He has coauthored over 60 articles in well-reputed international journals and over 16 (U.S. or W.O.) patents. His current research interests include mobile terminal mm-wave antennas, biological effects, CubeSat antennas, massive multiple-input and multiple-output (MIMO) antenna arrays, ultra-wideband (UWB) wind turbine blade deflection sensing, and RFID antennas.

Zhinong Ying (SM'05) joined Sony Mobile Communication AB, Lund, Sweden, in 1995, and became a Senior Specialist in 1997 and an Expert in 2003 in his engineer career, where he is currently a Principle Engineer of antenna technology in the Access Technology Laboratory, Research and Technology Division, and a Distinguish Engineer within the whole Sony Group. He also has been a Guest Professor with the Joint Research Centre, KTH Royal Institute of Technology, Stockholm, Sweden, and Zhejiang University, Hangzhou, China, since 2001. He has authored and coauthored over 150 articles in various kinds of journal, conference, and industry publications. He holds more than 150 patents and pending in the antennas and new generation wireless network areas. He contributed several book chapters on mobile antenna, small antenna, and multiple-input and multiple-output (MIMO) antennas in "Mobile Antenna Handbook 3rd edition" edited H. Fujimoto and "Handbook of Antenna Technologies" edited by Z. N. Chen. He had contributed a lot of work in antenna designs and evaluation methods for the mobile industry. He has also involved in the evaluation of Bluetooth technology, which was invented by Ericsson. His current research interests include small antennas, broad and multiband antenna, multichannel antenna (MIMO) system, antenna for body area network, antenna and propagation in fifth-generation mobile network, including massive MIMO and mm-wave, near-field and human body effects, and measurement techniques.

Dr. Ying was a member of the Scientific Board of Antenna Center of Excellent in the European 6th Frame Program from 2004 to 2007. He was a recipient of the Best Invention Award at Ericsson Mobile in 1996 and the Key Performer Award at Sony Ericsson in 2002. He was nominated for the President Award at Sony Ericsson in 2004 for his innovative contributions. He was also a recipient of the Distinguish Engineer title at Sony Group in 2013. He served as a TPC Co-Chairman for the International Symposium on Antenna Technology in 2007, a session organizer of several international conferences, including the IEEE APS, and a reviewer for several academic journals.
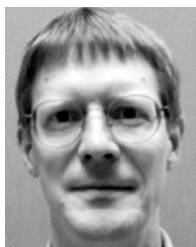
Arthur S. Morris, III (S'90–M'91–SM'04–F'13) received the B.S. degree in physics and in electrical engineering and the M.S. and Ph.D. degrees in electrical engineering from North Carolina State University, Raleigh, NC, USA, in 1983, 1986, and 1993, respectively.

He has contributed to device technologies ranging from traveling-wave tubes to millimeter-wave heterojunction bipolar transistors and has developed products for markets from high-voltage instrumentation to broadband communication systems as a scientist/engineer with a concentration on physical electronics and electromagnetic fields for over 30 years. In 1999, he joined Coventor, Inc., Raleigh, NC, USA, to lead software and hardware development to drive the transition of microelectromechanical systems (MEMS) and microsystems from the laboratory into products for RF and optical applications. He was a Cofounder of Wispry Inc., Irvine, CA, USA, which spun out of Coventor in 2002. He is currently the company's Chief Technical Officer and leads the development of high-performance programmable RF products for high-volume markets utilizing MEMS, CMOS, and advanced packaging.

Gert Frølund Pedersen was born in 1965. He received the B.Sc. and E.E. (Hons.) degrees in electrical engineering from the College of Technology in Dublin, Dublin Institute of Technology, Dublin, Ireland, in 1991, and the M.Sc.E.E. and Ph.D. degrees from Aalborg University, Aalborg, Denmark, in 1993 and 2003, respectively.

Since 1993, he has been with Aalborg University, where he is currently a Full Professor heading the Antennas, Propagation, and Millimeter-Wave Systems Laboratory with 25 researchers. He is also the Head of the Doctoral School on wireless communication with some 40 Ph.D. students enrolled. He has also worked as a Consultant for developments of more than 100 antennas for mobile terminals, including the first internal antenna for mobile phones in 1994 with lowest specific absorption rate (SAR), first internal triple-band antenna in 1998 with low SAR and high total radiated power (TRP) and total isotropic sensitivity (TIS), and recently various multiantenna systems rated as the most efficient on the market. He has worked most of the time with joint university and industry projects. He have received more than 21M\$ in direct research funding. He is currently the Project Leader of the RANGE project with a total budget of over 8M\$ investigating high-performance centimeter-/millimeter-wave antennas for 5G mobile phones. He has been one of the pioneers in establishing over-the-air measurement systems. The measurement technique is now well established for mobile terminals with single antennas and he was chairing the various COST groups with liaison to 3GPP and CTIA for over-the-air test of multiple-input and multiple-output (MIMO) terminals. He is currently involved in MIMO OTA measurement. He has authored or coauthored more than 500 peer-reviewed articles, six books, and 12 book chapters. He holds over 50 patents. His current research interests include radio communication for mobile terminals especially small antennas, diversity systems, propagation, and biological effects.